Biosensors and Bioelectronics 179 (2021) 113043

Contents lists available at ScienceDirect

Biosensors and Bioelectronics

journal homepage: http://www.elsevier.com/locate/bios

The hot-wire concept: Towards a one-element thermal biosensor platform

Mehran Khorshid [*,1], Soroush Bakhshi Sichani [1], Peter Cornelis, Gideon Wackers, Patrick Wagner [**]

KU Leuven, Department of Physics and Astronomy, Laboratory for Soft Matter and Biophysics, Celestijnenlaan 200 D, B-3001, Leuven, Belgium

ARTICLE INFO

Keywords:
Label-free bio- and chemosensors
Nucleic acids
3ω principle
Thermal waves

ABSTRACT

In this work, the 3ω hot-wire concept is explored as a prospective biosensing platform with a single sensing element that can detect analytes based on a change in the thermal interface conductance. A uniform receptor layer such as single-stranded DNA is immobilized on a thin aluminium wire, which serves not only as an immobilization platform but also as a heating element and temperature sensor together. The wire is heated periodically with an alternating current (angular frequency ω) and the third harmonic (frequency 3ω) of the voltage across the wire renders the efficiency of heat transfer from the wire to the surrounding medium. The amplitude of the 3ω voltage depends sensitively on the composition and conformation of the biofunctional interface layer. We illustrate this with a model system that includes blank aluminium wires, wires with silanes bound covalently to the native surface oxide, and with single-, respectively double-stranded DNA tethered to the silanes. The difference in heat-transfer due to these coatings is significant and measurable not only in a liquid but also in air. Based on this proof-of-concept, various applications come in sight such as mutation analysis and analyte detection with aptamers or molecularly-imprinted polymers as receptors. Wire materials other than aluminium are possible as well and the concept is suitable for miniaturization and parallelization.

1. Introduction

Bio- and chemo-sensors have applications in various domains such as pharmacology, medical diagnostics, biology, and food safety (Aygun et al., 2017; Isenberg, 2012; Nirschl et al., 2011; Wang et al., 2012; Zimmermann et al., 2002; Van Dorst et al., 2010; Su et al., 2020; Yang et al., 2015; Zhang et al., 2017). To keep the assay times short, or to follow the concentration of biomolecular markers in real time, label-free and fast transducer principles are highly demanded. Generally, these transducers detect receptor-target interactions such as antibody-antigen recognition and DNA hybridization on the basis of physical interface properties such as optical-, acoustical-, electrochemical-, and thermal characteristics (Sang et al., 2013). Most widely known in this context are surface-plasmon resonance SPR (Homola et al., 1999), quartz-crystal microbalances QCM (Höök and Kasemo, 2006; Naklua et al., 2016), and a broad range of electrochemical techniques such as potentiometry, amperometry, cyclic voltammetry and impedance spectroscopy (Katz and Willner, 2003; Wang, 2006; De Wael et al., 2012; Poghossian et al., 2007).

Thermal transducers are comparatively rare and the majority of articles on this topic refers to calorimetric measurements on the reaction enthalpies of biomolecular interactions such as the melting-temperature analysis in DNA duplexes, as well as thermal monitoring of biomolecules (*e.g.* glucose, urea, penicillin G) using enzymatic reactions (Ansevin et al., 1976; Bataillard et al., 1993; Urban et al., 1991). Besides of heat capacity, thermal resistance (respectively conductance) is a second thermal parameter that can be used in a bio- and chemo-analytical context. One of the embodiments, the heat-transfer method HTM, was developed by co-authors of this article and the scheme of a "HTM device" is shown in Fig. 1A. Conceptually, it has similarities with impedance spectroscopy, with the difference that the electrical current is replaced by a thermal current and the role of the voltage is taken over by a temperature gradient. The technique lends itself to all applications that are hardly feasible with electrical detection principles such as in the case of electrically insulating chip materials, receptor coatings, and liquids. The application range of HTM is actually very broad and overviews can be found in refs. (Eersels et al., 2017; Khorshid et al., 2020; van Grinsven et al., 2014). A few selected examples include mutation analysis in DNA

* Corresponding author. Laboratory for Soft Matter and Biophysics ZMB, Celestijnenlaan 200 D, B-3001, Leuven, Belgium.
** Corresponding author. Laboratory for Soft Matter and Biophysics ZMB, Celestijnenlaan 200 D, B-3001, Leuven, Belgium.
E-mail addresses: Mehran.Khorshid@kuleuven.be (M. Khorshid), PatrickHermann.Wagner@kuleuven.be (P. Wagner).
[1] Both authors contributed equally.

https://doi.org/10.1016/j.bios.2021.113043
Received 2 October 2020; Received in revised form 21 January 2021; Accepted 23 January 2021
Available online 29 January 2021

(van Grinsven et al., 2012), the detection of neurotransmitters with molecularly imprinted polymers (Peeters et al., 2013), detection of allergenic proteins with aptamers (Peeters et al., 2015), the study of phase transitions in lipids (Losada-Pérez et al., 2014), and the selective quantification and qualification of mammalian cells (Eersels et al., 2013, 2015), and bacteria with surface-imprinted polymers (van Grinsven et al., 2016).

In all cases, the measured parameter is the heat-transfer resistance R_{th}, being the ratio between the temperature difference $T_1 - T_2$ between the heated backside of the chip and the supernatant liquid, and the heating power P, see Fig. 1A. Interestingly, the concept works also in an inverted design, in which the receptors are not immobilized on the chip but on the temperature sensor in the liquid as shown in Fig. 1B (Diliën et al., 2017). As a route towards parallelization, several thermocouples can be used that are functionalized with receptors for a variety of targets. Another variation to HTM is the thermal-wave transfer analysis TWTA in which the backside temperature T_1 of the chip displays a harmonic oscillation so that the penetration depth of the resulting thermal wave into the medium can be adjusted to experimental needs (Peeters et al., 2016; Steen Redeker et al., 2017). The underlying denominator for the applicability of HTM relies on the fact that heat transport from the solid chip to the liquid (or from a liquid to a thermocouple) through an interlayer depends sensitively on the molecular-vibration properties of this interlayer (Khorshid et al., 2020). Binding of ligands or entire cells to on-chip receptors or on-chip DNA denaturation are evidently processes in which the vibrational properties of this interlayer will change.

While these thermal-resistance biosensors are widely applicable and further optimizations are ongoing, we point out that HTM is still not easy to implement in a portable, handheld device because a stable room temperature is essential to obtain accurate data. Furthermore, the method requires that the liquid is stagnant during the analysis to obtain a defined temperature gradient, which complicates potential in-line applications in *e.g.* a production process. Finally, it is not trivial to derive absolute values of the thermal-interface resistance because steady-state techniques are affected by parasitic heat losses and a calibration step is necessary to determine the heating-power fraction that bypasses the interface between chip and liquid (Zhao et al., 2016; Khorshid et al., 2020).

In this perspective, we explore in the present work whether simplifications are possible, to start with the number of physical elements that are involved in generating the output signal. In the given examples, there are three input parameters entering the R_{th} value, being the two temperatures T_1 and T_2 (often measured with thermocouples) and the heating power P. Uncertainties on these three parameters add up in a cumulative uncertainty and also in this perspective it seems promising to reduce the number of elements; not in the least, a high signal-to-noise ratio is beneficial to obtain low limits of detection.

Fig. 1C shows the concept of a 2ω device with two on-chip meanders made of chromium (Reyes-Romero et al., 2014): One meander, the sender, is connected to an alternating, sinusoidal voltage with angular frequency ω ($f = 40$ Hz), which generates oscillations of the emitted power with frequency 2ω. This thermal wave is picked up by the second meander (the receiver) and due to its thermal coefficient of resistance (TCR), the voltage $U_{2\omega}$ measured along the receiver oscillates at 2ω ($f =$ 80 Hz) when feeding it with a low and constant probing current. The concept was used to study the proliferation of bacterial cultures (*Enterococcus faecalis*) and the amplitude of $U_{2\omega}$ reflects the thermal diffusivity of the chip-to-liquid interface: Upon culture growth to a confluent layer, less heat was dissipated to the liquid, resulting in larger amplitudes of $U_{2\omega}$. This method requires two elements, sender and receiver, and two elements are also used in a modified version of HTM that is illustrated in Fig. 1D: A single on-chip meander serves as power source and temperature sensor for T_1 (chip-backside temperature) together while the temperature of the liquid (T_2) was measured with a calibrated Pt100 resistor. This way, the detection limit of HTM for *E. coli* bacteria could be brought down from initially 10^4 CFU (colony forming units) per ml to 100 CFU/ml in a complex matrix (Cornelis et al., 2019; van Grinsven et al., 2016).

The logical next step would be to reduce the number of involved elements even further, from two to one, and this brings us to a single wire or a single meander. Since on-chip meanders still lose a fraction of

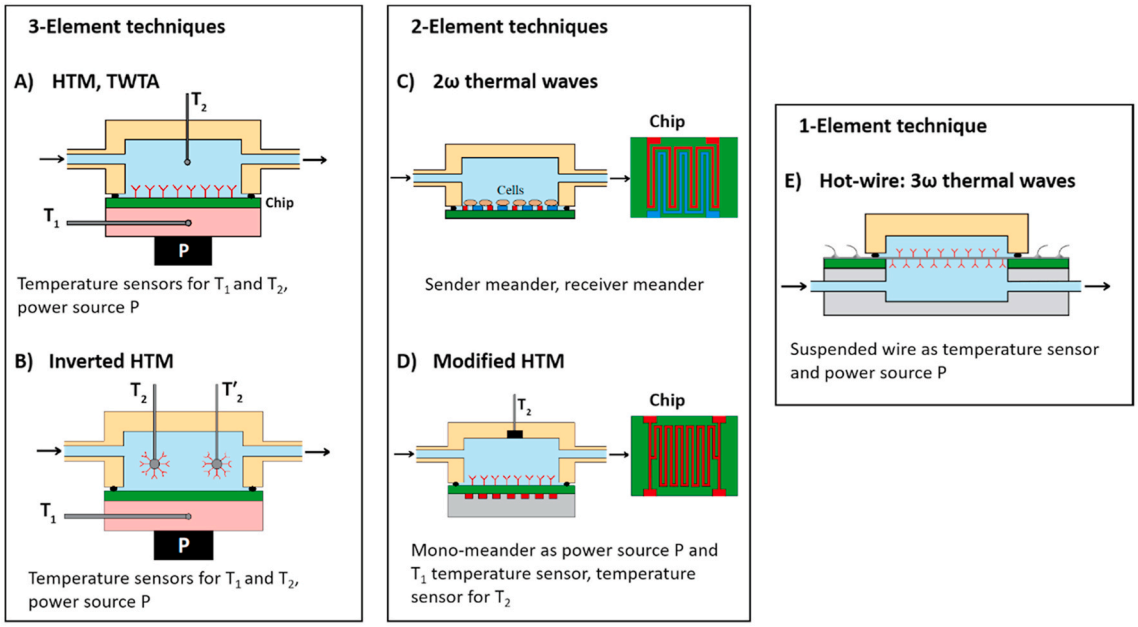

Fig. 1. Schematics of various thermal biosensor designs: A) Conventional layout for the heat transfer method HTM and thermal-wave transfer analysis TWTA with the receptor layer on a planar chip, power source P and two temperature sensors for T_1 and T_2, resulting in a three-element technique. The receptor symbol is meant in a generic sense and represents all kinds of receptors. B) Inverted HTM with the receptors immobilized on thermocouples in the liquid as a way towards parallelization. C) The 2ω technique with two on-chip meanders uses two elements: the sender and the receiver of a thermal wave. D) Modified HTM with a single meander that serves as heater and temperature sensor, together with the temperature sensor for T_2 this is a two-element technique. E) The 3ω principle uses only one element, the single wire serves as immobilization platform for receptors, as power source and as thermometer.

their heating power along the chip, we decided for freely suspended wires that are fully surrounded by liquid. This way, the generated heat necessarily passes the solid-liquid interface completely without parasitic heat losses. In order to probe the heat transfer from solid to liquid, we will employ the 3ω method, which is classically used to determine the heat capacity and thermal conductivity of solids and liquids (Cahill, 1990; Wang and Sen, 2009; Lee, 2009; Heinz et al., 2020; Vogel-Schäuble et al., 2013), as wells as the interface thermal conductance of ultrathin films (Wang et al., 2006; Chien et al., 2008; Lee and Cahill, 1997; Lee et al., 2009; Guermoudi et al., 2020). In the 3ω method, an alternating current of angular frequency ω causes power- and temperature oscillations with 2ω based on Joule heating. This results in periodic changes of the resistance with frequency 2ω and a voltage signal that oscillates with the frequency 3ω at an amplitude in the milli-Volt range. The calculations regarding the magnitude of $U_{3\omega}$ are given in the Supporting Information SI 1, based on literature references (Dames, 2013; Dames and Chen, 2005; Lu et al., 2001). In brief, $U_{3\omega}$ represents the efficiency of heat transfer from the wire to the medium in the sense that poor heat transfer (such as a wire in air) results in high $U_{3\omega}$ amplitudes while $U_{3\omega}$ is low in case of good thermal coupling and efficient removal of Joule's heat. In the references on the 3ω technique given above, $U_{3\omega}$ was smaller than U_{ω} (at the fundamental frequency) by typically three orders of magnitude and, to obtain nevertheless clear $U_{3\omega}$ signals, wire materials should be chosen with high TCR values such as gold or aluminium (Jaber and Chapuis, 2018).

Since the 3ω-based hot-wire technique is used as a biosensing platform with a functional surface layer, several boundary conditions need to be considered to obtain a reliable response. First, the wire material should be biocompatible while the current amplitude and the resistance of the wire (determined by its length, diameter, and material) should be chosen in a way to avoid extreme temperatures beyond the tolerance of biological samples. Furthermore, the layer under study should be insulating to avoid parasitic electrical currents. Moreover, to have a stable medium temperature during the measurement, the volume of the medium should be sufficiently large (Schiffres and Malena, 2011). Finally, it is important that the thickness of the functional coating is much smaller than the thickness of the wire itself and small in comparison to the thermal penetration depth: This way, the heat flow through the coating can be treated as one-dimensional heat propagation in case of on-chip heaters and as a radial heat-flow situation for suspended wires (Guermoudi et al., 2020).

To best of our knowledge, the 3ω method has not yet been combined with receptor functionalities, hence there are no 3ω–type biosensors yet, but the principle is well established in for instance the context of physical sensors, crystallography (Xu et al., 2019), nanotechnology (Barako et al., 2015), and health care (Natesan and Bischof, 2017). Exemplary applications include measuring the flow speed of liquids (Heyd et al., 2010), the analysis of gas mixtures and gas pressure (Kommandur et al., 2015; Assael et al., 2010), thermal conductivity analysis of biological tissues and cell suspensions (Lubner et al., 2015; Park et al., 2014), and monitoring the formation of bacterial biofilms (Clausen et al., 2017). For completeness, we mention that the transient plane source TPS is another thermal sensing principle, that employs only a single sensing element, see (Maqsood et al., 1994). As an example, Park and co-workers utilized the TPS principle successfully to determine the denaturation temperature of bovine serum albumin in solution, but this is a physical sensor in the sense that there were no receptor functionalities involved (Park et al., 2011).

2. Experimental

2.1. Chemical products

Analytical grade absolute ethanol (purity $\geq$ 99.8%) was purchased from Fisher Scientific (Merelbeke, Belgium). Technical grade isopropanol (purity $\geq$ 99%) and acetone (purity 99%) were obtained from VWR (Oud-Heverlee, Belgium). The silane, N-[3-Trimethoxysilyl)propyl]-ethylenediamine triacetic acid trisodium salt, 45% in water with –COOH termination was purchased from abcr GmbH (Karlsruhe, Germany). Acetic acid (purity 99.5%), used as a catalyst for silanization, was bought from Riedel-de Haën AG (Seelze, Germany). N-(3-dimethylaminopropyl)-N′-ethylcarbodiimide hydrochloride (EDC), and 2-(N-morpholino)ethanesulfonic acid (MES) powder were both purchased from Sigma-Aldrich (Overijse, Belgium) and used for EDC coupling. The silane layer serves as a covalently acting linker to the native surface oxide of aluminium and its –COOH terminus enables to graft probe DNA using the EDC reaction (Christiaens et al., 2006). There are many more covalent functionalization routes for oxide surfaces documented in literature, an overview can be found in the review article by Pujari et al. (2014). The buffer 0.1 × PBS with pH 7.4 was made with Milli-Q (MQ) water and contained 12.90 mM sodium chloride NaCl (purity $\geq$ 99%), 0.62 mM anhydrous sodium phosphate dibasic Na_2HPO_4, and 0.15 mM potassium phosphate monobasic KH_2PO_4 (purity $\geq$ 99.8%), all from Sigma-Aldrich. We used 0.1 × PBS on purpose because its salinity is low enough to avoid corrosion of the aluminium wire. This dilution is mentioned as "PBS" throughout the article. 10 × PCR buffer used for DNA hybridization was purchased from New England Biolabs (Hitchin, UK). Aluminium wire-bonding wire with 1% silicon and 30 μm diameter (42.4 Ω/m) was obtained from Heraeus Electronics (Hanau, Germany) and used as the core sensing element. Single-stranded DNA (ss-DNA) was purchased from Integrated DNA Technologies IDT (Leuven, Belgium). The amine-terminated probe DNA had the sequence 5′-NH_2–C_6H_{12} - AAA AAA ACC CCT GCA GCC CAT GTA TAC CCC CGA ACC - 3'. The target DNA, with a Cy3 fluorescent label to verify hybridization optically, was fully complementary to the probe and had the sequence 5' - Cy3 - $C_6H_{14}O_4$ - GGT TCG GGG GTA TAC ATG GGC TGC AGG GG - 3'. The seven adenine nucleotides at the 5′ terminus of the probe DNA served as a spacer to reduce steric hindrance during the hybridization step.

2.2. Silanization of the Al micro-wires

Aluminium is always surrounded by a native, dense oxide layer with a typical thickness in the order of 5–10 nm (Revie and Uhlig, 2008), which can serve for silanization. Using x-ray diffraction and Rutherford backscattering, we confirmed the presence of this surface oxide in the expected thickness range. This surface oxide is stable at neutral pH ranges (Alexander et al., 2016), and the surface oxidation is a self-limiting process (Cai et al., 2012). The micro-wires (cut in 6 cm long pieces) were washed first with acetone and then with isopropanol in the sonicating bath, for 10 min each, and dried with N_2 gas. Then, two wires were fixated by soldering on a printed circuit board (PCB) inside the flow-through sensing compartment that is described in Section 2.6. The silanization was performed directly inside the sensing compartment, which was filled with 600 μl of the silane liquid and 60 μl of acetic acid and incubated for 2 h at room temperature. Then, the liquid was removed from the reservoir and the wires were washed by flushing them several times with MQ water and subsequently with absolute ethanol. To avoid hydrolyzation of the –COOH groups on the silane layer, the wires were kept in absolute ethanol until further use. The complete workflow, including also the subsequent steps, is illustrated in Fig. 2.

2.3. Grafting of probe DNA and hybridization with target DNA

After drying the silanized wires with N_2 gas, they were incubated in a mixture of 30 μl –NH_2 terminated probe ss-DNA (concentration 100 pmol/μl) in 270 μl MQ and 300 μl of 50 mg/ml EDC solution in 25 mM MES buffer (pH 6) for 150 min in the dark at 4 °C. EDC accelerates the amide-bond formation between the –COOH end group of the silanes and the –NH_2 termination of the probe ss-DNA. Afterwards, we rinsed the wires three times with PBS to remove unbound ss-DNA and kept them in PBS at 4 °C until further modifications. For the hybridization step, the

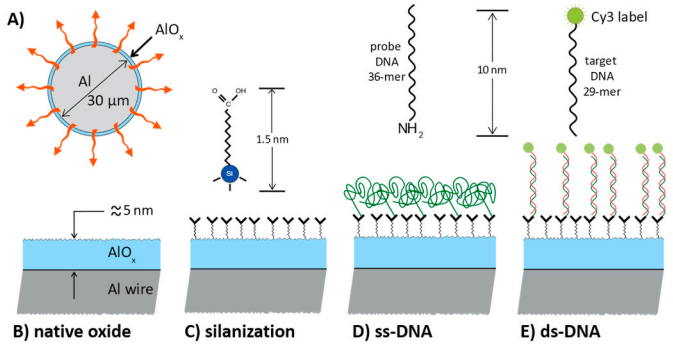

Fig. 2. Schematic representation of the architecture of coatings on the aluminium micro-wires. A) Scheme of the aluminium wire in cross section, the red arrows indicate the direction of heat propagation to the surrounding medium, being air or PBS buffer. B) Boundary interface covered by native surface oxides that serve for electrical insulation toward the liquid and as a base layer for bio-chemical functionalization. C) Functionalization with the silanes, used as cross-linkers for coupling DNA to the hot wire. The terminal –COOH groups show vibrational overlapping (O–H stretching) with surrounding water molecules, facilitating heat transfer. D) Attachment of single-stranded probe DNA (36 nucleotides) by EDC coupling between the –COOH groups of the silanes and the amino-modification at the 5′ terminus of the ss-DNA. E) Hybridization with complementary target DNA (29 nucleotides), featuring a fluorescent Cy3 marker at the 5′ site. Hybridization alters the conformation of DNA from random coils (ss-DNA) to stiff rods (ds-DNA). (For interpretation of the references to colour in this figure legend, the reader is referred to the Web version of this article.)

PBS buffer was removed and the wires were incubated in an aqueous solution containing 100 μl of Cy3-labeled complementary ss-DNA (with a concentration of 1000 pmol/μl) diluted in 500 μl of 1 × PCR buffer for 2 h in oven at 35 °C. Afterwards, the wires were rinsed three times by flushing with PBS to remove non-hybridized target DNA. The wires were stored in PBS at 4 °C until the actual 3ω measurements.

Since the purpose of our work is to distinguish between different types of bio-functional layers on basis of their heat-transfer characteristics, it is important to assess the impact of each additional layer step by step. Therefore, the 3ω analysis was performed on four different types of coatings in the following sequence, see Fig. 2: A, B) Blank aluminium wires with only their native oxide coating, C) wires functionalized with a monolayer of silane linkers, D) wires with probe DNA attached to the silanes, and E) wires on which the probe DNA was hybridized with complementary target DNA. For each coating type, the 3ω measurements were done at least three times in order to enhance the statistics. Note here that these repetitions were independent experiments, each with a newly prepared wire. To ensure reproducibility, all wires were from the same bonding-wire spool and the active length of each wire was carefully kept constant. All wires were tested in air and in PBS to assess the effect of different surrounding media on the thermal transport behavior through the functionalized layers.

2.4. Microscopic surface characterization after DNA immobilization

To verify the DNA immobilization, fluorescence imaging was carried out with a Olympus IX 81 fluorescence microscope (Olympus, Tokyo, Japan), equipped with a 25 mW laser at 532 nm wavelength combined with an Orca-Flash 40 CCD camera (Hamamatsu Photonics K.K., Hamamatsu City, Japan) to record the fluorescence signals. Furthermore, atomic force microscopy was performed to estimate the surface density of DNA grafted to the Al-wire surface. For this, we used an Agilent 5500 AFM with MAC Mode III module, operated in the Alternating Current Atomic Force Microscopy (ACAFM) mode in air at room temperature (cantilever: MSNL-F cantilever with 120 kHz resonance frequency and 0.6 N/m spring constant).

2.5. The principle of the 3ω method

In the present work, we used the 3ω method as a low-noise, transient technique to characterize, respectively to identify bio-molecular interface layers based on their thermal conductance properties. Within this section, we explain the relationship between the amplitude of the 3ω voltage and the thermal resistance of this interlayer. Due to the complexity of the calculations, we limit the description to the most important steps, the full derivation is given in the Supporting Information SI 1; for topical literature we refer to (Dames, 2013; Dames and Chen, 2005; Lu et al., 2001). The cylindrical Al micro-wires used as the central sensing element were connected to the auxiliary instruments in 4-point geometry as shown in Fig. 3A. This geometry allows to avoid possible contributions by contact resistances. The two outer contacts on the printed circuit board were used to heat up the wire by feeding an A. C. current $I_0 \cos(\omega t)$ while the two inner contacts on the PCB were connected to record the voltage along the wire. I_0 is the current amplitude passing through the wire at the angular frequency ω. The total length of the wire between the voltage contacts was 25 mm, a 13 mm segment of the wire was freely surrounded by the liquid, corresponding therefore to the active length of the sensing probe. The ohmic resistance of the active part was 1.01 Ω for a D.C. current at room temperature (19 °C). The alternating current induces Joule heating in the wire based on the power dissipation according to Equation (1):

$$P = R_0 I^2(t) = \frac{1}{2} R_0 I_0^2 (1 + \cos(2\omega t)) \quad (1)$$

This power rises the temperature of the wire by $\Delta T(t)$ with respect to the ambient temperature T_0 and $\Delta T(t)$ consists of two parts: A steady component T_{DC} that would also be there with a constant D.C. current I_0 and a contribution with amplitude $|T_{2\omega}|$ that oscillates with the frequency 2ω. The full time dependence of ΔT is given by Equation (2):

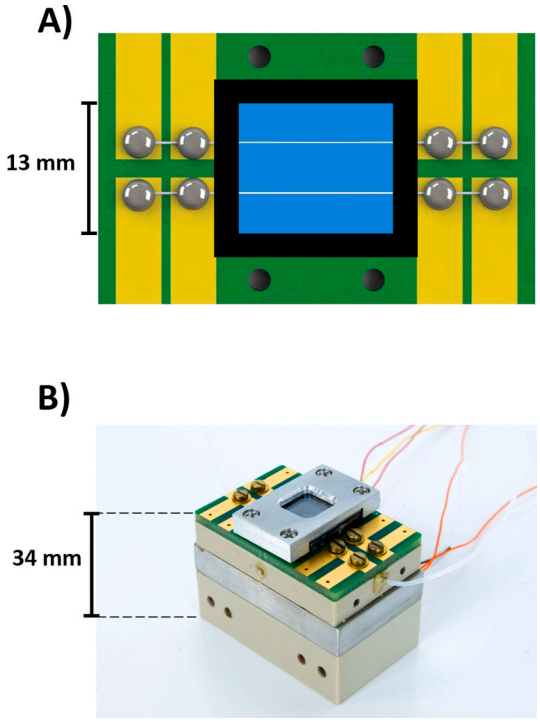

Fig. 3. Flow-cell compartment for the hot-wire technique. A) Schematic top view of the hot-wire flow cell showing that the wires are freely suspended in the liquid under study. The aluminium wires have 30 μm diameter and 13 mm active length. B) Photograph of the hot-wire device, hosting the flow-cell compartment with two independent aluminium wires contacted in four-point configuration by using a printed circuit board. Panel A) is a drawing because the wires would not be visible at this scale.

$$\Delta T(t) = T(t) - T_0 = T_{DC} + |T_{2\omega}|\cos(2\omega t + \phi_{2\omega}) \quad (2)$$

In the oscillatory part of the temperature, the phase angle $\phi_{2\omega}$ represents the lag between the sinusoidal temperature fluctuations of the wire and the power that is dissipated from the wire to the ambient. Furthermore, the electrical resistance of the wire follows the temperature oscillations due to the temperature coefficient of resistance (here with symbol β) and R_0 in Equation (3) is the initial resistance at ambient temperature. The 3ω voltage signal can be measured with a lock-in amplifier and it is directly proportional to the temperature oscillation at the second harmonic according to Eq. (3) (Lu et al., 2001).

$$|U_{3\omega}| = \frac{1}{2} R_0 I_0 \beta \, |T_{2\omega}| = \frac{1}{2} U_0 \beta \, |T_{2\omega}| \quad (3)$$

Since U_0 is the first harmonic voltage ($U_{1\omega}$) along the wire, the amplitude of the temperature oscillation $|T_{2\omega}|$ can be calculated based on the geometry and the structure of the wire. The thermal characteristics of the solid-liquid interface and the medium around the wire can be derived from analyzing the wire-temperature oscillations. The thermal energy spreads fast through a medium with a high thermal conductivity κ (hence low-amplitude $|T_{2\omega}|$ fluctuations) while $|T_{2\omega}|$ will be large in case that heat dissipation from the wire to the ambient is hampered by *e.g.* a thermally insulating coating. To determine the thermal conductivity κ of the sample, the complete solution for radial heat diffusion from a line heater (radius r_0) in an infinitely long, cylindrical medium is used (Acquaroli, 2018). As a result, the thermal conductivity of the medium surrounding a wire with radius r_0 can be calculated with Equation (4).

$$\kappa = \frac{\beta R_0^2 I_0^3}{8\pi l_h |U_{3\omega}|} \frac{K_0(qr_0)}{qr_0 K_1(qr_0)} \Rightarrow |U_{3\omega}| \sim \beta \frac{I_0^3}{\kappa} \quad (4)$$

In this equation, l_h is the length of the wire, β is its TCR, and q represents the thermal wave number, which is proportional to the frequency and thermal diffusivity α of the layer. K_0 and K_1 stand for the zeroth- and the first-order modified Bessel function of the second kind. From Eq. (4), we see directly that the 3ω voltage is proportional to the TCR of the wire material (for aluminium $\beta = 0.00429\ ^\circ C^{-1}$) (Rahman et al., 2019), to the third power of the imposed heating current I_0, and inversely related to the thermal conductivity κ. It is clear that the derived κ value is sensitive to several parameters that are the TCR of the heater, the initial resistance, the applied current, the effective length of the wire, and the radius of the wire. For a detailed calculation of the sensitivity of κ to each of these parameters, we refer to the Supporting Information SI 2. We point out that this derivation does not explicitly take into account the thermal boundary resistance between the wire and the medium, therefore κ should be seen as an effective quantity that comprises the boundary resistance and the thermal conductivity of the medium itself. Furthermore, $U_{3\omega}$ is in approximation (ignoring the Bessel function) proportional to r_0^{-5}, which means that only a thin wire can bring about sufficiently high 3ω voltages.

2.6. Flow-cell compartment and instrumentation

Fig. 3B shows the flow-cell compartment with an inner volume of 1.25 ml, it is made of the chemically resilient polymer PEEK (polyetherether ketone) while the top- and bottom lids consist of glass. The bottom plate and the metal cap are made of aluminium to obtain an efficient thermal coupling to the ambient; all measurements were carried out at 19 °C room temperature. The device can currently host two wires for a minimal redundancy and upgrades to more wires are possible. The wires are fixed on a printed circuit board, see Fig. 3A, with four contacts per wire and a central opening of 100 mm^2.

To fix the wires we soldered them to the contacts with tin containing acidic flux medium to remove the electrically insulating AlO_x coating. By comparing the electrical four-point and two-point resistance, we verified that the contact resistance cannot be higher than 10 mΩ, which ensures that there is no Joule heating at the contacts. This has been further confirmed by temperature monitoring of the contacts by using a Testo 868 thermal camera (Testo LTD., Hampshire, UK), which showed that the temperature of the contacts did not exceed 26 °C. It is worth mentioning that the resistance between two blank Al wires inside the flow-cell that was filled with 0.1 × PBS, is ca. 100 kΩ. This indicates a good electrical insulation effect by the oxide coating, and the wires did not show visual degradation after being kept for at least 12 h in 0.1 × PBS. The functionalization steps described in Sections 2.2, 2.3 were done with the wires already installed on this PCB, however outside the flow cell to limit the use of chemicals. For the actual measurements, the PCB with the wires was sandwiched between the lower and the upper part of the flow cell with a square-shaped silicone-rubber seal. The flow cell has inlet- and outlet tubing, allowing for facile injection or exchange of different fluids.

To heat up the Al wires, a voltage-to-current amplifier (BOP 72-3M, KEPCO Inc., Flushing, New York, USA) was connected to the outer electrodes of the PCB. The A.C. current was modulated by a SR850 DSP dual phase lock-in amplifier (Stanford Research Systems, Sunnyvale, California, USA), which was controlled by a LabVIEW 2017 program, version 17.0 (National Instruments Corp., Austin, Texas, USA). The electrical current passing through the wire was monitored in real-time with a 34401A multimeter (Hewlett-Packard, Palo Alto, California, USA), see Supporting Information SI 3. The voltage electrodes of the wire were connected to the SR850 lock-in amplifier to filter and measure three different harmonics (ω, 2ω, 3ω) of the voltage signal individually. With this setup, the frequency f ($= \omega/2\pi$) in the range from 7 Hz to 100 Hz was swept by the lock-in amplifier with different voltages as an input for the linear voltage-to-current amplifier (BOP 72-3M) with the gain $g_m = I_{out}/V_{in} = 300$ mA/V. The A.C. current with amplitude I_0 in the range from 0 to 400 mA for 0.1 × PBS and 0 to 250 mA for air with 50 mA increments was applied to the wire and the three harmonics of voltage signal were analyzed. The indicated frequency and current ranges were determined experimentally to bring about discernible $U_{3\omega}$ signals for the chosen wire geometry with 13 mm active length and 30 μm diameter; however, we suppose that these parameters are transferable to other lengths and diameters as long as the resulting resistance stays in a similar order. The threshold current at which the wire will break by local overheating is ca. 650 mA for air as surrounding medium.

3. Results and discussion

3.1. Microscopic characterization of DNA immobilization process on Al wire

The successful immobilization of DNA molecules on Al wires was confirmed by fluorescence microscopy. As explained in Section 2.1, the fluorescent Cy3-labels were attached to the 5' terminus of the complementary target strands; Cy3 has its absorbance maximum (excitation peak) at the wavelength 554 nm and the emission maximum is at 568 nm. Fig. 4 shows the fluorescence-microscopy images of a blank Al wire

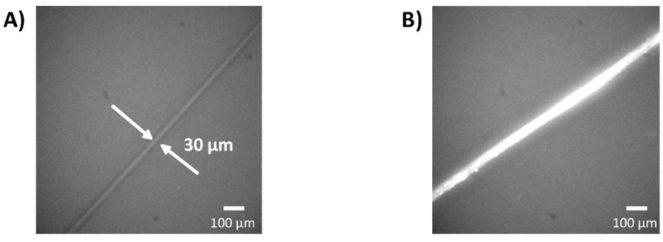

Fig. 4. Fluorescence microscopy images of Al wires with 30 μm diameter, A) prior to functionalization and covered only with the native surface oxide (blank) and B) after being functionalized with double-stranded DNA in which the target strains are fluorescently labeled with Cy3 dyes at the 5′ terminus.

prior to functionalization and after hybridization to ds-DNA, which was performed directly on the wire. It is important to note that from the fluorescent intensity we cannot calculate the areal density of DNA duplexes. Therefore, we characterized the surface for different Al-wire coatings using an Agilent 5500 AFM in dry mode (see Supporting Information SI 4). An inspection based on AFM imaging revealed that the areal density is at least 1.4×10^{11} duplexes per cm^2. This is in the same order as reported by Murib et al. (2016), who used x-ray photoemission spectroscopy to determine the areal density of ds-DNA (same fragment length as in our case) grafted with silanes on synthetic sapphire (Al_2O_3) chips.

3.2. Heat transfer in different surrounding media

First, the applicability of the Al micro-wires for the 3ω principle was tested in air and in PBS: The heat-transfer efficiency from the wire to the medium should be substantially different when comparing a gas to a liquid. Fig. 5 shows $U_{3\omega}$ as a function of the effective current I_{RMS} ($I_{RMS} = I_0/\sqrt{2}$) through a blank, non-functionalized wire at the frequency $f = 7$ Hz. All given $U_{3\omega}$ values refer to the root-mean square (RMS) of the 3ω voltage. As will be discussed further in Section 3.3, frequencies above 7 Hz result in lower 3ω voltages; below 7 Hz, there is a comparatively high noise on the data and these frequencies are therefore not considered in the analysis.

For the case of air in Fig. 5A, we see that $U_{3\omega}$ is proportional to the third power of the current I_0, which agrees perfectly with Eq. (4) in Sect. 2.5. The fit based on the function $U_{3\omega} = A \times I_0^3$ has a goodness factor $R^2 = 0.997$, $\chi^2 = 1.46 \times 10^{-8}$, with $A = 0.341 \pm 0.007$ (V/A^3). The measurements for each current were performed in triplicate (three complete measuring rounds) and the error bars are the standard deviations. In each measuring round, we started at 7 Hz and employed the full series of currents from 100 to 250 mA before moving to the next higher frequency (10 Hz) to repeat the same series of currents. This scheme was continued up to the highest frequency of 100 Hz. Measuring an individual data point (a given current and frequency, without repetition) took 30 s in total, being 10 s for each of the voltages $U_{1\omega}$, $U_{2\omega}$, and $U_{3\omega}$. Only in case of $f = 7$ Hz, a 10 s waiting time was used prior to recording the voltages to guarantee a stable thermal-wave signal, for frequencies of 10 Hz and higher the voltage signals were constant in less than a second. Supporting Information SI 7 shows the evolution of $U_{3\omega}$ as a function of time, illustrating the stability of the signal after 1 s in air and 0.5 s in 0.1 × PBS (at 7 Hz). It is important to note that according to Eq. S4 the voltage signal along the wire consists only of U_ω and $U_{3\omega}$ contributions. The $U_{2\omega}$ signal exists, but it is independent of the current and, according to our measurements at least 10 times lower than $U_{3\omega}$. Therefore, $U_{2\omega}$ was not used for further analysis. In an application case in which only $U_{3\omega}$ is important, the technique can provide 1 data point in less than 10 s, meaning that the concept can be considered for continuous-monitoring applications.

In view of the envisaged bioanalytical applications, it is of considerable interest to know the permanent temperature rise T_{DC} and the amplitude $|T_{2\omega}|$ of the temperature fluctuations around T_{DC}, T_0 denotes the ambient temperature. Both parameters can be calculated from the data by using Equations (5a) and (5b), in which β stands again for the TCR of the wire material; for the mathematical details we refer to the Supporting Information SI 1:

$$a)\ T_{DC} - T_0 = \frac{1}{\beta}\left(\frac{U_{1\omega}}{I_0 R_0} - 1\right) \qquad b)\ |T_{2\omega}| = \frac{2|U_{3\omega}|}{\beta |U_{1\omega}|} \tag{5}$$

As seen in Fig. 5A for air, T_{DC} increases rapidly with I_{RMS} and a current of 250 mA is already sufficient to obtain $T_{DC} = 64$ °C with oscillations of $|T_{2\omega}| = 8.1$ °C. We note that these temperatures are the results of measured data ($U_{1\omega}$, $U_{3\omega}$) combined with calculations (Eq. 5a, b), in which we assume that the wire temperature is homogeneous inside the wire; it is possible that the absolute wire temperature at its surface is lower. Since we will study thermal transport through ds-DNA in Section 3.3, it is important to stay below its melting temperature, which is 68 °C in air and in PBS as specified on the data sheet by the supplier of the DNA fragments.

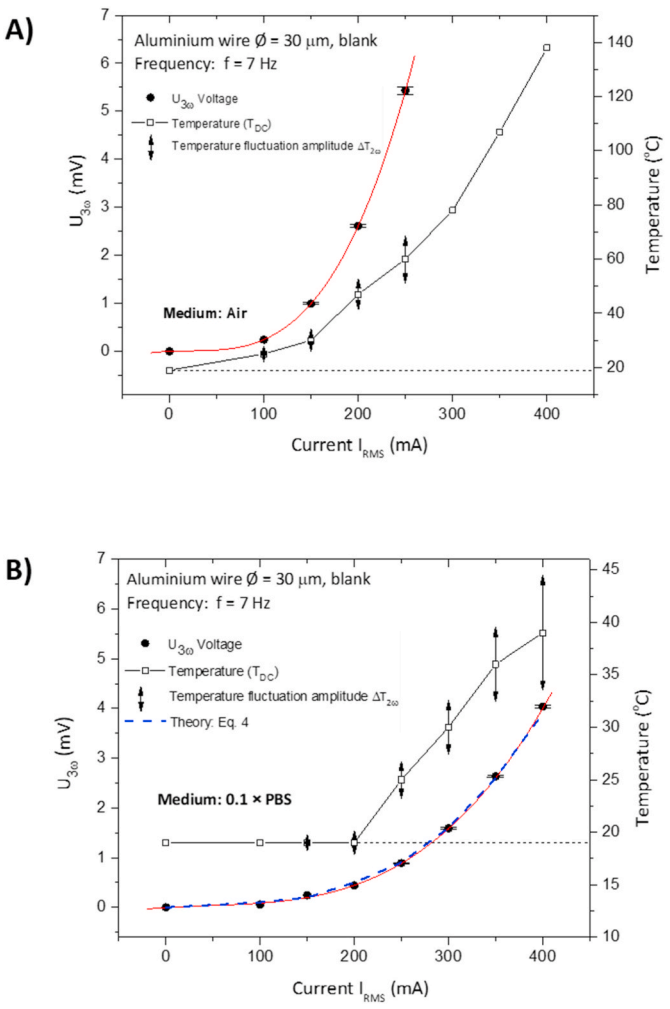

Fig. 5. Root-mean square of the 3ω voltage $U_{3\omega}$ and the DC temperature T_{DC} of a blank aluminium wire as a function of the current I_{RMS} for the fixed frequency $f = 7$ Hz. Panel A) shows the data for air as surrounding medium and panel B) for PBS buffer solution. The 3ω voltages (solid dots) are averages of three independent measurements; the error bars indicate the standard deviation, which can be smaller than symbol size. The solid lines through the $U_{3\omega}(I_{RMS})$ data are fits based on Eq. (4), rendering the proportionality to the third power of the current. The blue dotted line shows the perfect agreement between data and calculations based on Eq. (4). Comparing the data in A) and B) for a given current, the higher $U_{3\omega}$ for air shows its less efficient heat transfer from the wire to the ambient as compared to PBS. This is also visible in the DC temperatures T_{DC} (calculated with Eq. 5a), given as open boxes that are connected with a guide to the eye, error bars are smaller than symbol size. The vertical arrows around the T_{DC} data represent the temperature fluctuations $|T_{2\omega}|$obtained with Eq. 5b. The ambient temperature is indicated with a dotted line at 19 °C. The temperature fluctuation of the wire in air was not measured for currents above 250 mA to stay below the denaturation temperature of ds-DNA molecules. (For interpretation of the references to colour in this figure legend, the reader is referred to the Web version of this article.)

In case of the PBS buffer in Fig. 5B, we see again the characteristic proportionality between $U_{3\omega}$ and the third power of I_0 with $R^2 = 0.998$, $\chi^2 = 3.28 \times 10^{-9}$, and $A = 0.062 \pm 0.001$ (V/A^3), with the difference that the absolute $U_{3\omega}$ values are "damped" and roughly five times lower in comparison to air for any given current. Regarding the case of PBS in Fig. 5B, the current dependence of $U_{3\omega}$ can actually be calculated

directly from Eq. (4) without using any fit parameters. The calculated curve agrees perfectly with the data when using for water $\kappa = 0.62$ W/m.K, $\alpha = 0.146 \times 10^{-6}$ m^2/s, q $= 24.55 \times 10^3$ m^{-1}, $l_0 = 13$ mm, $R_0 = 1.01$ Ω, and $r_0 = 15 \times 10^{-6}$ m (Popiel and Wojtkowiak, 1998).

For air it is not possible to calculate $U_{3\omega}$ (I_0) with Eq. (4) because q itself shows a strong temperature dependance. For currents up to $I_{RMS} \leq$ 200 mA, the DC temperature cannot be distinguished from room temperature while $I_{RMS} = 400$ mA results in $T_{DC} \approx 39$ °C; even when taking $|T_{2\omega}| = 5.4$ °C into account, this stays safely below the melting temperature. Furthermore, the rise of the temperature of the medium during the measurement is far less than 2.4 °C as shown in Fig. S4 in the Supporting Information SI 8. For the experiments on ss- and ds-DNA coatings, we decided for $I_{RMS} = 250$ mA for air as surrounding medium and $I_{RMS} = 400$ mA for PBS. A high current is evidently beneficial for the signal-to-noise ratio with which $U_{3\omega}$ (in the milli-Volt range) can be measured, but there are practical limitations: Currents of 500 mA and more in PBS cause a risk that the wire breaks spontaneously. The reason seems to be that the voltage drop along the suspended part of the wire exceeds the insulating properties of the native oxide layer; once the insulating oxide breaks down at any point along the wire, the aluminium core dissolves by electrochemical corrosion.

3.3. Heat transfer through different (bio-)molecular coatings

As outlined in Sect. 2.5, the 3ω method probes the thermal conductivity κ of the medium surrounding the wire and, with some modifications, one can also obtain the heat capacity (Dames and Chen, 2005; Gauthier et al., 2013; Grosse et al., 2018; Jaber and Chapuis, 2018). The concept does not take explicitly into account that there is a thermal boundary resistance between dissimilar materials (*e.g.* a metal in contact with a liquid), but it is clear that the four, additive wire coatings (native oxide, silanes, ss- and ds-DNA) represent four physically different interfaces between aluminium and the surrounding air or PBS. In this sense, the measured $U_{3\omega}$ values are "effective data" that depend on a superposition of the medium properties and the interface properties. Since the medium is always the same (either air or PBS), changes in $U_{3\omega}$ due to a specific coating directly indicate a change in the heat-transfer mechanism between the wire and the medium. Fig. 6 shows $U_{3\omega}$ for the four different wire coatings in contact with either air (panel A) or with PBS (panel B) in the frequency range from f = 7–100 Hz. The current amplitude was fixed to 250 mA for air in order not to exceed the melting temperature of DNA and in PBS we opted for 400 mA, high enough to obtain a good signal-to-noise ratio while still avoiding wire breakdown. The magnitude of $U_{3\omega}$ decreases systematically with increasing f and this can actually be predicted from Eq. (4), where the frequency is embedded implicitly in the Bessel functions via the thermal wavenumber q, which is frequency dependent. If necessary to increase the signal amplitude even more, it seems useful to employ trigger frequencies lower than 7 Hz, but we could not obtain stable signals with the available instrumentation (see Supporting Information SI 9); note here that HTM as described in the Introduction is a zero-frequency method due to its steady-state character. Interestingly, the $U_{3\omega}(f)$ traces for a given medium do not cross, which means that the efficiency of heat transfer from the wire to the medium depends only on the coating itself but not on the applied frequency. In the following discussion, we focus therefore on the data for $f = 7$ Hz, without loss of generality.

Fig. 6C shows $U_{3\omega}$ for the four different coating types in PBS at 7 Hz as a function of the applied current I_{RMS}. These data were fitted with Eq. (4), leaving only the thermal conductivity κ as the free parameter. This way, we obtained $\kappa = 0.606 \pm 0.008$ W/m.K for the blank aluminum wire, which is in remarkably good agreement with the literature value of 0.602 W/m.K for pure water at 20 °C (Popiel and Wojtkowiak, 1998). In case of the other coatings, the thermal conductivities are nominal values, because the coating itself modulates the heat-transfer efficiency. For the silanized wire, we found $\kappa = 0.686 \pm 0.009$ W/m.K, and for the DNA functionalized wires the respective data are 0.518 ± 0.010 W/m.K (ss-DNA) and 0.569 ± 0.009 W/m.K (ds-DNA). The perfect agreement with literature in case of the blank wire gives confidence that the device and methodology outlined in the Experimental Section fulfill all boundary conditions for obtaining accurate 3ω data. The uncertainty margins shown in Fig. 6C are again standard deviations of three independent measurement and all fits had R^2 values of at least 0.996.

For a facile comparison of the impact of the different coatings, Fig. 6D summarizes the data at $f = 7$ Hz from Fig. 6A and B as bar charts: In the case of air as surrounding medium, the data seem straightforward to interpret: There is no clear difference between a blank and a silanized wire, $U_{3\omega}$ is slightly higher for the silanized version, but this effect falls within the rather narrow error bars that represent the standard deviation of three independent measurements. The length of individual silane molecules is ca. 1.5 nm, vanishingly small in comparison to the wire diameter, and we can safely assume that the surface area is unaltered. Furthermore, it is established that silanes form rigid molecular monolayers (Haensch et al., 2010). With single- and double-stranded DNA however, there is a pronounced increase of $U_{3\omega}$: Taking the silanized wires as a reference point with $U_{3\omega} = 5.46$ mV, this value increases to 6.91 mV for ss-DNA and to 8.10 mV for ds-DNA. These effect sizes exceed the width of the error bars (typically ± 0.05 mV) by far and it is certainly surprising when comparing this to the dimensions of the fragments: The stretched-out length of the probe DNA is 12.2 nm for the 36 nucleotides including the 7 adenine groups of the spacer. The target DNA with 29 nucleotides measures ca. 9.9 nm in length. Since DNA can only form monolayers in our coupling scheme, the thickness of the DNA layer is still vanishingly small in comparison to the wire diameter and the $U_{3\omega}$ increase must therefore indicate a change in the heat-transfer mechanism from the wire to the ambient air. At least for ss-DNA, which was grafted in an aqueous phase, one can expect a highly disordered, and entangled structure because the fragments are longer than the persistence length $l_P = 3$ nm reported for a 25 mM NaCl solution (Ambia-Garrido et al., 2010; Murphy et al., 2004). Hence, heat from the wire cannot propagate directly from the solid to the air, but has to pass a soft-matter interlayer in which thermal transport neither resembles the mechanism in a solid (by phonons) nor in a gas (by collisions).

After hybridization, the fragments should become stiff because they are shorter than the persistence length $l_P \approx 50$ nm of ds-DNA, however we still expect disorder in the dried state: Despite of vigorous washing, it is likely that fragments stick to each other and to the wire surface due to remaining salt ions. The strength of the thermal insulation effect is in any case surprising, comparable to "fleece textile" and thermal superinsulating materials (for which DNA is not known yet) receive increasing attention in various engineering applications (Cuce et al., 2014).

Turning now to the case of PBS buffer in Fig. 6D, the first unexpected result is the drop of $U_{3\omega}$ due to the silane layer. It is evidently unrelated to a change in effective surface area, but it can be understood on basis of a hypothesis that we published earlier (Khorshid et al., 2020): The heat transfer from a solid to a liquid seems to rely, at least partly, on the transfer of vibrational energy between molecules, more specifically between molecules at the top layer of the solid and the molecules in the liquid. In the present case however, the chosen silanes have a carboxyl (-COOH) terminus in which the stretching vibrations of the –OH groups have the same frequency as –OH stretching in water molecules; the corresponding frequency range is 92.94–110.92 THz (Coates, 2006). This way, energy transfer becomes much more facile and efficient than by direct transfer from vibrations in the Al-surface oxide to water. Heat transfer between two different materials is not yet well understood on the basis of first principles, but non-radiative Förster resonance energy transfer FRET is a possible energy transfer channel that can take place when there is a frequency matching between the donor and the acceptor molecules (Andrews, 1989; Jares-Erijman and Jovin, 2003). The observation that certain ligands may enhance heat transfer (lower the thermal boundary resistance) was also made with time-domain thermoreflectance experiments (Tian et al., 2015). This technique is hardly applicable in a biosensor context due to the exceedingly high power

intensities of a pulsed laser.

When looking at DNA as an interlayer, the jump height of $U_{3\omega}$ from the silanized state to ss-DNA is 1.20 mV, only slightly less than in case of air but again substantially more than the width of the error bars with ±0.02 mV found in all measurements with PBS buffer. In an aqueous medium, the ss-DNA fragments are known to curl up in Flory spheres, which increases the surface coverage of the solid with organic material (van Grinsven et al., 2012). In turn, the clear increase in $U_{3\omega}$ in combination with the very limited uncertainties shows that the hot-wire principle has a surprisingly high sensitivity to surface processes at the

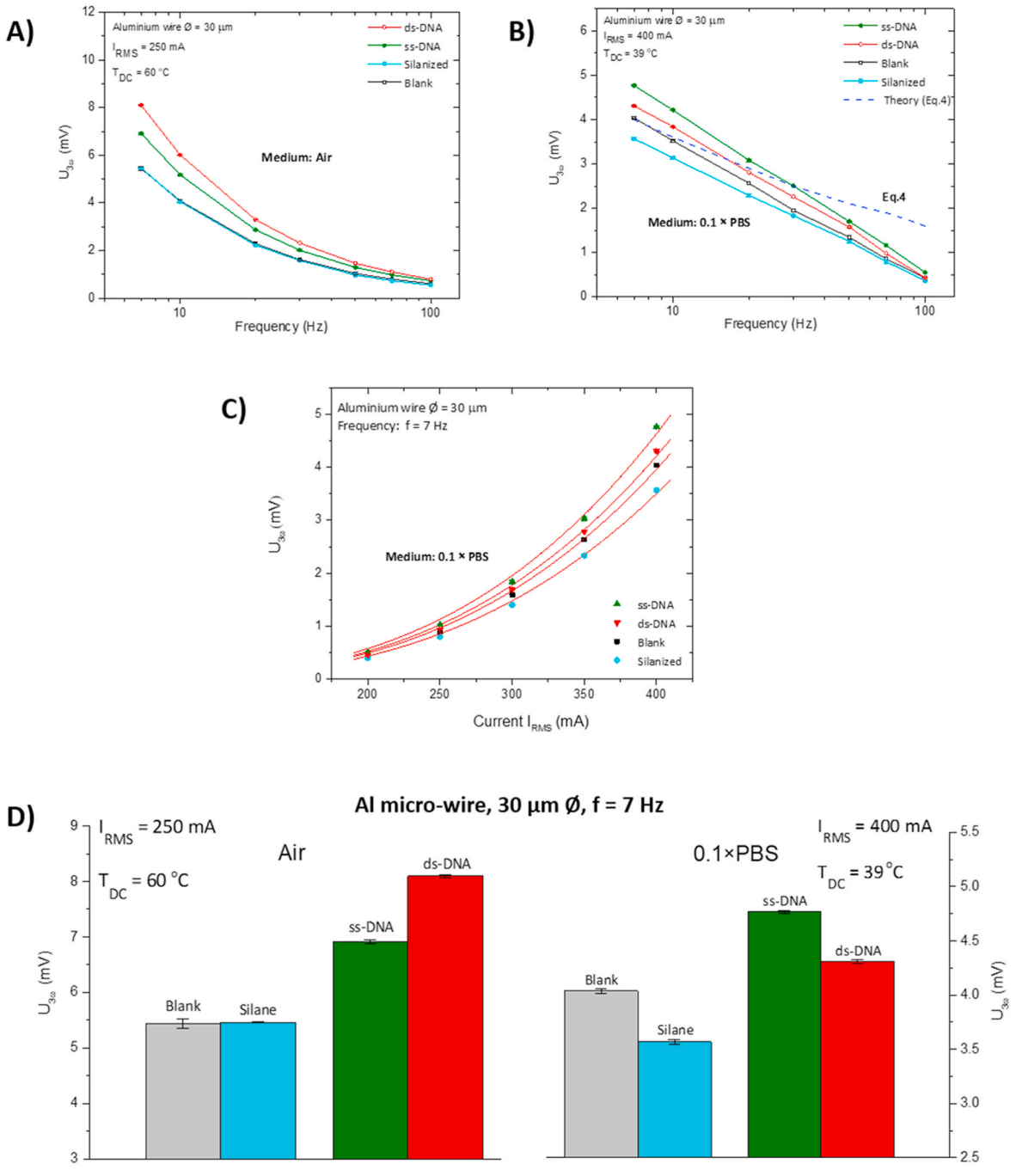

Fig. 6. Frequency dependence of $U_{3\omega}$ for a blank aluminium wire, a silanized wire, and wires functionalized with ss- or ds-DNA, using the silanes as linkers. Panel A) shows the data set for air as surrounding medium with $I_{RMS} = 250$ mA, the data for PBS are given in B) with $I_{RMS} = 400$ mA. All data points are averages of at least three measurements, the error bars are the standard deviations while certain error bars are smaller than the symbol size. Throughout, $U_{3\omega}$ decreases with increasing f while the general pattern how $U_{3\omega}$ depends on the coating type is the same for all frequencies. The frequency dependence of $U_{3\omega}$ for PBS shows overall a good agreement with values calculated with Eq. (4), which is given as a dotted blue line. C) Current dependence of $U_{3\omega}$ at 7 Hz for the different coatings in PBS; the fit curves are calculated with Eq. (4) to determine the thermal conductivity κ of the aqueous medium as a cross-check for the accuracy of the methodology. D) Bar charts of $U_{3\omega}$ for the different surface types in air or PBS at $f = 7$ Hz. In case of air, silanes have no effect on $U_{3\omega}$ while ss- and ds-DNA cause a strong $U_{3\omega}$ increase, illustrating their thermal insulation effect. With PBS, the silanes facilitate heat transfer from the wire to the ambient due to vibrational matching with water molecules. Single-stranded DNA with its random-coil structure reduces the heat-transfer efficiency while ordered brushes of ds-DNA promote thermal transport. All error bars are considerably smaller than the effect sizes and all observations hold for other currents and frequencies. (For interpretation of the references to colour in this figure legend, the reader is referred to the Web version of this article.)

molecular level. Since molecular-scale alterations at a surface are inherent to all affinity-based biosensors, we speculate that the hot-wire technique can eventually be useful for a plurality of applications. The final step to ds-DNA goes along with a drop of $U_{3\omega}$ by 0.46 mV. Technically speaking, this is 23 times more than the width of the uncertainty margins and the fact of a drop instead of an increase can again be understood in terms of surface coverage (van Grinsven et al., 2012; Murib et al., 2016). While ss-DNA forms random coils, possibly with mutual entanglement, hybridization results in stiff rods, upright on the wire surface, and within the aqueous phase there is no reason to assume a disorder stabilized by salt residues. An upright orientation of the duplexes creates open space between neighboring fragments so that the silanized Al wire is again locally in direct contact with the liquid medium. Here, we point out that the surface coverage addressed in Sect. 3.1 is well below its hypothetical limit of 10^{13} duplexes per cm^2, hence still allowing to alter the surface coverage by hybridization or denaturation without steric hindrance.

4. Summary and conclusions

Amongst the established transducer principles found in biosensors, there is a small subgroup that employs thermal resistance effects at solid-liquid interfaces with the receptor functionalities being immobilized at this interface. The principle is known from literature for various receptor types, including single-stranded probe DNA, aptamers, molecularly imprinted polymers and surface imprinted polymers. This allows for a wide variety of bioanalytical applications in which the targets are detected selectively and quantitatively in real time without the need for labelling agents. Notwithstanding, heat-transfer biosensors did not yet make the step towards real-life applications and commercial availability because of hindering factors: These are the need for a temperature-controlled environment, difficulties regarding parallelization, and time delay to establish a stable temperature gradient within the liquid under study. The sample fluid must also be stagnant, which is a disadvantage for in-line monitoring. To overcome these limitations, we made in this work an attempt to integrate the four separate components of heat-transfer measurements (receptor chip, power source and two temperature sensors) into a single element. This element, the "hot-wire", serves as a power source, immobilization platform and temperature sensor together; with the choice for commercial aluminium micro-wires that are ubiquitously used in the electronics industry, the hot-wire is an especially cheap element.

To assess whether such approach is technically feasible and whether it is sufficiently surface-sensitive to changes at the molecular (nanoscale) level, the proof-of-concept addressed a model situation with a stepwise buildup of the interface: From blank aluminium with only its native oxide layer, *via* a linker layer of silanes, to single-stranded DNA and finally complementary duplexes of double-stranded DNA. As a quantitative indicator for the heat-transfer efficiency from the hot-wire to the ambient (air and PBS buffer as a model fluid), we used the 3ω thermal-wave technique in which the voltage at the third harmonic of the triggering frequency entails the heat-transfer properties of the (bio-) molecular coating. As a practical result, we found that silane monolayers enhance heat transfer from the wire to the buffer considerably due to an overlap in the molecular vibration modes of the silanes' carboxyl group with water molecules. Single-stranded DNA layers with their entangled morphology strongly impede thermal transport while hybridization to stiff double helices makes heat transfer again measurably more efficient. While this confirms earlier results obtained with the steady-state heat-transfer method, the progress is not only in the drastic reduction of sensing elements (from four to one), but also in surprisingly low noise levels. Furthermore, the signal generation is quasi instantaneous at the scale of seconds without need for thermal stabilization; this is appealing to monitor dynamic processes as a function of time and the low thermal mass of the wire is an asset for a rapid detection scheme. It may also be of interest to control the absolute temperature of the wire to support or to inhibit certain processes at its surface; this can be achieved *via* adapting the triggering current while the amplitude of the temperature fluctuations can be controlled through the chosen frequency ω.

Starting from this proof-of-concept to establish the operational parameters of the method, it seems promising to work towards real proofs-of-application: First, we point out that the wires can consist of any conducting material that has a reasonably high thermal coefficient of resistance. Aluminium was chosen for its native oxide layer that isolates the wire electrically from the liquid while it served also as an anchoring point for silane-based linking chemistry. There are many more self-passivating metals with surface-oxide layers, including titanium and tantalum that are used in medical implants for their biocompatibility and resilience against corrosion in a wide pH- and salinity range. Gold micro-wires, electrically isolated with a dense monolayer of thiol linkers, might be useable in the same way. It is worth to note that various surface-chemical functionalization routes are available. A facile approach to graft receptors to micro-wires is the functionalization from solution, which is common practice for *e.g.* nucleic acids, aptamers, antibodies and certain types of molecularly imprinted polymers. This micro-wire has an especially low surface area, which should allow detecting low molecular concentrations when the wire is for instance coated with molecularly imprinted polymers as receptors. For applications in which the shape of the wire might be important, it is clear that a straight wire can also be wound to a tiny coil or loop. Such micro-wires will have advantages for measurements on tiny sample volumes, for instance in the context of microfluidics. If further miniaturization is required, one may think about the very small dimensions of nanowires that are known for instance in the context of field-effect based biosensor arrays.

Author contributions

M.K. and S.B.S. designed experiments and performed the "hot-wire" measurements. The "3ω method" instrumentation and "hot-wire" setup were designed and calibrated by P.W., M.K., S.B.S., P.C., and G.W. P.C. developed the LabView programming. S.B.S., M.K., and P.W. performed interpretation and data analysis. M.K., S.B.S., and P.W. wrote the manuscript. All authors have given approval to the last version of the manuscript.

Declaration of competing interest

The authors declare that they have no known competing financial interests or personal relationships that could have appeared to influence the work reported in this paper.

Acknowledgements

The authors kindly acknowledge the Research Foundation Flanders FWO for making this work possible through the project G0791.16N "Utilizing interfacial impedance- and heat-transfer phenomena in advanced monitoring- and switching devices" and the bilateral FWO Flanders – FWF Austria project "Simultaneous multiparametric readout for low-cost nanoparticle sensors". Furthermore, P. Cornelis was supported in the initial phase of this work by an internal FLOF fellowship of the Special Research Funds BOF of KU Leuven. We wish to thank Dr. O. Deschaume and Profs. C. Bartic, M. J. Van Bael, A. Vantomme, and J. Van de Vondel (all in KU Leuven) for their technical support, providing AFM images and the surface-analytical characterization of the aluminium micro-wires. Furthermore, we appreciate stimulating scientific discussions on thermal-wave sensors with Prof. C. Glorieux (KU Leuven) and Prof. P. Lieberzeit at the University of Vienna. The sensing device was manufactured by the technicians W. Neefs, J. Vandamme, P. Mispelter, and V. Tuts at KU Leuven.

Appendix A. Supplementary data

Supplementary data to this article can be found online at https://doi.org/10.1016/j.bios.2021.113043.

References

Acquaroli, L.N., 2018. arXiv preprint arXiv, 1811.00571. Webpage. www.arxiv.org/abs/1811.00571. retrieved on Oct. 02, 2020.
Alexander, S., Gomez, V., Barron, A.R., 2016. J. Nanomater. 8, 2016, art. no. 7950876.
Ambia-Garrido, J., Vainrub, A., Pettitt, B.M., 2010. Comput. Phys. Commun. 181, 2001–2007.
Andrews, D.L., 1989. Chem. Phys. 135, 195–201.
Ansevin, A.T., Vizard, D.L., Brown, B.W., McConathy, J., 1976. Biopolymers 15, 153–174.
Assael, M.J., Antoniadis, K.D., Wakeham, W.A., 2010. Int. J. Thermophys. 31, 1051–1072.
Aygun, U., Avci, O., Seymour, E., Urey, H., Ünlü, M.S., Ozkumur, A.Y., 2017. ACS Sens. 2, 1424–1429.
Barako, M.T., Roy-Panzer, S., English, T.S., Kodama, T., Asheghi, M., Kenny, T.W., Goodson, K.E., 2015. ACS Appl. Mater. Interfaces 7, 19251–19259.
Bataillard, P., Steffgen, E., Haemmerli, S., Manz, A., Widmer, H.M., 1993. Biosens. Bioelectron. 8, 89–98.
Cahill, D.G., 1990. Rev. Sci. Instrum. 61, 802–808.
Cai, N., Zhou, G., Müller, K., Starr, D.E., 2012. Appl. Phys. Lett. 101, 4, 171605.
Chien, H.C., Yao, D.J., Huang, M.J., Chang, T.Y., 2008. Rev. Sci. Instrum. 79, 7, 054902.
Christiaens, P., Vermeeren, V., Wenmackers, S., Daenen, M., Haenen, K., Nesládek, M., vandeVen, M., Ameloot, M., Michiels, L., Wagner, P., 2006. Biosens. Bioelectron. 22, 170–177.
Clausen, C., Pedersen, T., Bentien, A., 2017. Sensors 17 (552), 12.
Coates, J., 2006. Interpretation of infrared spectra, a practical approach. In: Meyers, R.A. (Ed.), Encyclopedia of Analytical Chemistry: Applications, Theory and Instrumentation. John Wiley & Sons Ltd., Chichester, pp. 10815–10837.
Cornelis, P., Givanoudi, S., Yongabi, D., Iken, H., Duwé, S., Deschaume, O., Robbens, J., Dedecker, P., Bartic, C., Wübbenhorst, M., Schöning, M.J., Heyndrickx, M., Wagner, P., 2019. Biosens. Bioelectron. 136, 97–105.
Cuce, E., Mert Cuce, P., Woor, C.J., Riffat, S.B., 2014. Renew. Sustain. Energy Rev. 34, 273–299.
Dames, C., 2013. Annu. Rev. Heat Transf. 16, 7–49.
Dames, C., Chen, G., 2005. Rev. Sci. Instrum. 76, 14, 124902.
De Wael, K., Daems, D., Van Camp, G., Nagels, L.J., 2012. Anal. Chem. 84, 4921–4927.
Diliën, H., Peeters, M., Royakkers, J., Harings, J., Cornelis, P., Wagner, P., Steen Redeker, E., Banks, C.E., Eersels, K., van Grinsven, B., Cleij, T.J., 2017. ACS Sens. 2, 583–589.
Eersels, K., van Grinsven, B., Ethirajan, A., Timmermans, S., Jiménez Monroy, K.L., Bogie, J.F.J., Punniyakoti, S., Vandenryt, T., Hendriks, J.J.A., Cleij, T.J., Daemen, M. J.A.P., Somers, V., De Ceuninck, W., Wagner, P., 2013. ACS Appl. Mater. Interfaces 5, 7258–7267.
Eersels, K., van Grinsven, B., Khorshid, M., Somers, V., Püttmann, C., Stein, C., Barth, S., Diliën, H., Bos, G.M.J., Germeraad, W.T.V., Cleij, T.J., Thoelen, R., De Ceuninck, W., Wagner, P., 2015. Langmuir 31, 2043–2050.
Eersels, K., van Grinsven, B., Peeters, M., Cleij, T.J., Wagner, P., 2017. Heat transfer as a new sensing technique for the label-free detection of biomolecules. In: Schöning, M. J., Poghossian, A. (Eds.), Label-Free Biosensing. Springer, Cham, pp. 383–407.
Gauthier, S., Giani, A., Combette, P., 2013. Sensors Actuators A Phys 195, 50–55.
Grosse, C., Abo Ras, M., Varpula, A., Grigoras, K., May, D., Wunderle, B., Chapuis, P.-O., Gomès, S., Prunnila, M., 2018. Sensors Actuators A Phys 278, 33–42.
Guermoudi, A.A., Cresson, P.Y., Ouldabbes, A., Boussatour, G., Lasri, T., 2020. J. Therm. Anal. Calorim. 143, 1–12.
Haensch, C., Hoeppener, S., Schubert, U.S., 2010. Chem. Soc. Rev. 39, 2323–2334.
Heinz, S., Chavez Angel, E., Trapp, M., Kleebe, H.-J., Jakob, G., 2020. Nanomaterials 10, vol. 1239, p. 12.
Heyd, R., Hadaoui, A., Fliyou, M., Koumina, A., Ameziane, L.E.H., Outzourhit, A., Sabougni, M.L., 2010. Rev. Sci. Instrum. 81, 044901, 6.
Homola, J., Yee, S.S., Gauglitz, G., 1999. Sensor. Actuator. B Chem. 54, 3–15.
Höök, F., Kasemo, B., 2006. The QCM-D technique for probing biomacromolecular recognition reactions. In: Steinem, C., Janshoff, A. (Eds.), Piezoelectric Sensors. Springer, Berlin, Heidelberg, pp. 425–447.
Isenberg, G., 2012. Modern Optics, Electronics and High Precision Techniques in Cell Biology. Springer, Berlin, Heidelberg.
Jaber, W., Chapuis, P.O., 2018. AIP Adv. 8, 13 art. no. 7396.
Jares-Erijman, E.A., Jovin, T.M., 2003. Nat. Biotechnol. 21, 1387–1395.
Katz, E., Willner, I., 2003. Electroanalysis 15, 913–947.
Khorshid, M., Losada-Pérez, P., Cornelis, P., Dollt, M., Ingebrandt, S., Glorieux, C., Renner, F.U., van Grinsven, B., De Ceuninck, W., Thoelen, R., Wagner, P., 2020. Sensor. Actuator. B Chem. 310, 127627.
Kommandur, S., Mahdavifar, A., Hesketh, P.J., Yee, S., 2015. Sensors Actuators A Phys 233, 231–238.
Lee, B., Lee, J.S., Kim, S.U., Kim, K., Kwon, O., Lee, S., Kim, J.H., Lim, D.S., 2009. J. Vac. Sci. Technol. B Microelectron. Nanometer. Struct. Process. Meas. Phenom. 27, 2408–2412.
Lee, S.-M., 2009. Rev. Sci. Instrum. 80, 7, 024901.
Lee, S.M., Cahill, D.G., 1997. J. Appl. Phys. 81, 2590–2595.
Losada-Pérez, P., Jiménez-Monroy, K.L., van Grinsven, B., Leys, J., Janssens, S.D., Peeters, M., Glorieux, C., Thoen, J., Haenen, K., De Ceuninck, W., Wagner, P., 2014. Phys. Status Solidi Appl. Mater. Sci. 211, 1377–1388.
Lu, L., Yi, W., Zhang, D.L., 2001. Rev. Sci. Instrum. 72, 2996–3003.
Lubner, S.D., Choi, J., Wehmeyer, G., Waag, B., Mishra, V., Natesan, H., Bischof, J.C., Dames, C., 2015. Rev. Sci. Instrum. 86, 12, 014905.
Maqsood, A., Amin, N., Maqsood, M., Shabbir, G., Mahmood, A., Gustafsson, S.E., 1994. Int. J. Energy Res. 18, 777–782.
Murib, M.S., Yeap, W.S., Eurlings, Y., van Grinsven, B., Boyen, H.G., Conings, B., Michiels, L., Ameloot, M., Carleer, R., Warmer, J., Kaul, P., Haenen, K., Schöning, M. J., De Ceuninck, W., Wagner, P., 2016. Sensor. Actuator. B Chem. 230, 260–271.
Murphy, M.C., Rasnik, I., Cheng, W., Lohman, T.M., Ha, T., 2004. Biophys. J. 86, 2530–2537.
Naklua, W., Suedee, R., Lieberzeit, P.A., 2016. Biosens. Bioelectron. 81, 117–124.
Natesan, H., Bischof, J.C., 2017. ACS Biomater. Sci. Eng. 3, 2669–2691.
Nirschl, M., Reuter, F., Vörös, J., 2011. Biosensors 1, 70–92.
Park, B.K., Yi, N., Park, J., Choi, T.Y., Lee, J.Y., Busnaina, A., Kim, D., 2011. Appl. Phys. Lett. 99 (163702), 4.
Park, B.K., Yi, N., Park, J., Kim, Y., Kim, D., 2014. AIP Adv. 4, 8, 047120.
Peeters, M., Csipai, P., Geerets, B., Weustenraed, A., van Grinsven, B., Thoelen, R., Gruber, J., De Ceuninck, W., Cleij, T.J., Troost, F.J., Wagner, P., 2013. Anal. Bioanal. Chem. 405, 6453–6460.
Peeters, M., van Grinsven, B., Cleij, T.J., Jiménez-Monroy, K.L., Cornelis, P., Pérez-Ruiz, E., Wackers, G., Thoelen, R., De Ceuninck, W., Lammertyn, J., Wagner, P., 2015. ACS Appl. Mater. Interfaces 7, 10316–10323.
Peeters, M., van Grinsven, B., Foster, C.W., Cleij, T.J., Banks, C.E., 2016. Molecules 21, vol. 552, p. 14.
Poghossian, A., Abouzar, M.H., Amberger, F., Mayer, D., Han, Y., Ingebrandt, S., Offenhäusser, A., Schöning, M.J., 2007. Biosens. Bioelectron. 22, 2100–2107.
Popiel, C.O., Wojtkowiak, J., 1998. Heat Tran. Eng. 19, 87–101.
Pujari, S.P., Scheres, L., Marcelis, A.T., Zuilhof, H., 2014. Angew. Chem. Int. Ed. 53, 6322–6356.
Rahman, M.M., Noh, S., Kim, K.H., Kim, H., 2019. J. Phys. Conf. Ser. 1407, 012112, 4.
Revie, R.W., Uhlig, H.H., 2008. Corrosion and Corrosion Control, fourth ed. John Wiley & Sons Ltd., New Jersey.
Reyes-Romero, D.F., Behrmann, O., Dame, G., Urban, G.A., 2014. Sensors Actuators A Phys 213, 43–51.
Sang, S., Zhang, W., Zhao, Y., 2013. Review on the design art of biosensors. In: Rinken, T. (Ed.), State of the Art in Biosensors – General Aspects. InTech, Rijeka, pp. 89–110.
Schiffres, S.N., Malen, J.A., 2011. Rev. Sci. Instrum. 82, 7, 064903.
Steen Redeker, E., Eersels, K., Akkermans, O., Royakkers, J., Dyson, S., Nurekeyeva, K., Ferrando, B., Cornelis, P., Peeters, M., Wagner, P., Diliën, H., van Grinsven, B., Cleij, T.J., 2017. ACS Infect. Dis. 3, 388–397.
Su, Y., Wang, J., Wang, B., Yang, T., Yang, B., Xie, G., Zhou, Y., Zhang, S., Tai, H., Cai, Z., Chen, G., 2020. ACS Nano 14, 6067–6075.
Tian, Z., Marconnet, A., Chen, G., 2015. Appl. Phys. Lett. 106, 4, 211602.
Urban, G., Kamper, H., Jachimowicz, A., Kohl, F., Kuttner, H., Olcaytug, F., Goiser, P., Pittner, F., Schalkhammer, T., Mann-Buxbaum, E., 1991. Biosens. Bioelectron. 6, 275–280.
Van Dorst, B., Mehta, J., Bekaert, K., Rouah-Martin, E., De Coen, W., Dubruel, P., Blust, R., Robbens, J., 2010. Biosens. Bioelectron. 26, 1178–1194.
van Grinsven, B., Eersels, K., Akkermans, O., Ellermann, S., Kordek, A., Peeters, M., Deschaume, O., Bartic, C., Diliën, H., Steen Redeker, E., Wagner, P., Cleij, T.J., 2016. ACS Sens. 1, 1140–1147.
van Grinsven, B., Eersels, K., Peeters, M., Losada-Pérez, P., Vandenryt, T., Cleij, T.J., Wagner, P., 2014. ACS Appl. Mater. Interfaces 6, 13309–13318.
van Grinsven, B., Vanden Bon, N., Strauven, H., Grieten, L., Murib, M., Jiménez Monroy, K.L., Janssens, S.D., Haenen, K., Schöning, M.J., Vermeeren, V., Ameloot, M., Michiels, L., Thoelen, R., De Ceuninck, W., Wagner, P., 2012. ACS Nano 6, 2712–2721.
Vogel-Schäuble, N., Jaeger, T., Romanyuk, Y.E., Populoh, S., Mix, C., Jakob, G., Weidenkaff, A., 2013. Phys. Status Solidi Rapid Res. Lett. 7, 364–367.
Wang, H., Sen, M., 2009. Int. J. Heat Mass Tran. 52, 2102–2109.
Wang, J., 2006. Biosens. Bioelectron. 21, 1887–1892.
Wang, R.Y., Segalman, R.A., Majumdar, A., 2006. Appl. Phys. Lett. 89, 173113, 3.
Wang, Y., Wang, J., Yang, F., Yang, X., 2012. Anal. Chem. 84, 924–930.
Xu, R.L., Muñoz Rojo, M., Islam, S.M., Sood, A., Vareskic, B., Katre, A., Mingo, N., Goodson, K.E., Xing, H.G., Jena, D., Pop, E., 2019. J. Appl. Phys. 126, 7, 185105.
Yang, J., Chen, J., Su, Y., Jing, Q., Li, Z., Yi, F., Wen, X., Wang, Z., Wang, Z.L., 2015. Adv. Mater. 27, 1316–1326.
Zhang, N., Tao, C., Fan, X., Chen, J., 2017. J. Mater. Res. 32, 1628–1646.
Zhao, D., Qian, X., Gu, X., Jajja, S.A., Yang, R., 2016. J. Electron. Packag. 138, 1–19.
Zimmermann, B., Hahnefeld, C., Herberg, F.W., 2002. Targets 1, 66–73.